# iScience

## Article

# Alkali metal-linked triangular building blocks assemble a high-nucleation lanthanoid cluster based on single-molecule magnets



ns-4f Heterometallic Clusters
High-nucleation Clusters Based SMMs
High Stability & Assembly Mechanism

Dy$_3$K$_2$  Dy$_6$K$_2$  Dy$_{12}$Na$_6$  SMM

2 K   12 K    2 K   7 K    2 K   15 K

Yun-Lan Li, Hai-Ling Wang, Zhong-Hong Zhu, Xing-Lin Lu, Fu-Pei Liang, Hua-Hong Zou

18317725515@163.com (Z.-H.Z.)
fliangoffice@yahoo.com (F.-P.L.)
gxnuchem@foxmail.com (H.-H.Z.)

### Highlights

We synthesized ns-4f cluster-based SMM by using diamagnetic alkali metal connection

Clusters **1–3** are rare examples of ns-4f heterometallic clusters

Dy$_{12}$K$_6$ is currently the highest nuclear ns-4f heterometallic SMM

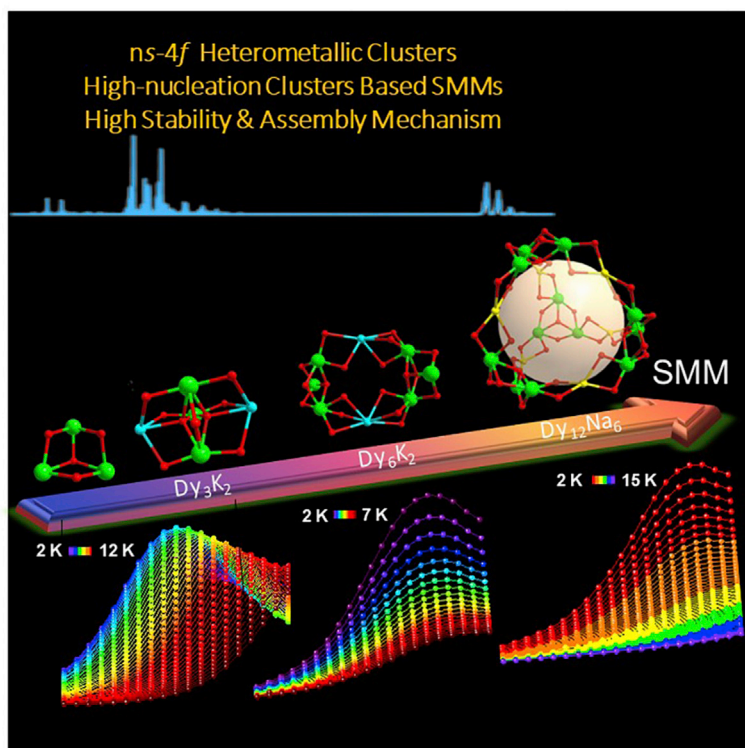HRESI-MS is used to explore the formation of ns-4f high-nucleation clusters

## Article

# Alkali metal-linked triangular building blocks assemble a high-nucleation lanthanoid cluster based on single-molecule magnets

Yun-Lan Li,[1] Hai-Ling Wang,[1] Zhong-Hong Zhu,[1,*] Xing-Lin Lu,[1] Fu-Pei Liang,[1,2,*] and Hua-Hong Zou[1,3,*]

## SUMMARY

**The metallic central magnetic axes in high-nucleation clusters with complex structural connections tend to be disorganized and cancel each other out. Therefore, high-nucleation clusters cannot easily exhibit single-molecule magnets (SMMs) behaviors. Herein, we select a triple-core building block ($Dy_3K_2$, 1) and use linked diamagnetic alkali metal to form an open, spherical, high-nucleation cluster $Dy_{12}Na_6$ (3) with SMM behavior. Furthermore, by changing the reaction conditions, $Dy_6K_2$ (2) formed by linking two $Dy_3$ by K(I) is obtained. High-resolution electrospray mass spectrometry of clusters 1–3 effectively captures the building block $Dy_3$, and clusters 1 and 3 and $Dy_3$ have high stability even with the increase in ion source energy. To the best of our knowledge, this is the first time that an SMM based on a high-nucleation cluster has been obtained by connecting magnetic primitives via diamagnetic metal ions. $Dy_{12}K_6$ is currently the highest nuclear ns-4f heterometallic SMM.**

## INTRODUCTION

Single-molecule magnets (SMMs), which belong to a remarkable class of molecular-based magnetic materials, have shown promising applications in molecular spintronic devices, high-density data storage, and quantum computing (Wernsdorfer and Sessoli, 1999; Meng et at., 2016; Zhang et al., 2013; Liu et al., 2016a; Bogani and Wernsdorfer, 2008). Lanthanoid ions have been confirmed as advanced spin carriers for SMMs because they possess unquenched orbital angular momentum and strong intrinsic magnetic anisotropy induced by strong spin–orbit coupling large magnetic moments (Woodru et al., 2013; Lu et al., 2017; Liu et al., 2016b; Hewitt et al., 2010; Ke et al., 2010). In particular, the Dy(III) ion, which has Kramer's ground state ($^6H_{15/2}$), inherently has a large magnetic moment and Ising-type magnetic anisotropy (Chen et al., 2016; Gupta et al., 2016; Durrant et al., 2022; Peng et al., 2021). In recent years, various strategies have been developed for the directional design of lanthanoid complexes to improve the turnover barrier ($U_{eff}$) and blocking temperature ($T_B$) of SMMs (Ungur et al., 2014; Pugh et al., 2016; Guo et al., 2022). In 2018, Tong and Richard A. Layfield et al. designed a ligand structure to tune the key structural parameters of the obtained dysprosium-based complexes to generate an axial crystal field that is strong enough to achieve the first breakthrough in $T_B$ liquid nitrogen temperature (up to 80 K) and $U_{eff}$ of up to 1541 cm$^{-1}$ (2217 K) (Guo et al., 2018a). In 2017, Nicholas F. Chilton et al. designed and synthesized the complex [Dy(Cp$^{ttt}$)$_2$][B(C$_6$F$_5$)$_4$] (Cp$^{ttt}$ = {C$_5$H$_2$$^t$Bu$_3$-1,2,4}, $^t$Bu = C(CH$_3$)$_3$) and observed a magnetic hysteresis phenomenon at a magnetic field scan rate of 22 Oe/s and $T_B$ of up to 60 K because of the local molecular vibration in the complex (Goodwin et al., 2017). In 2016, Zheng et al. selected Dy(III) as the spin carrier and designed and synthesized an SMM with a $U_{eff}$ as high as 1815 K and a $T_B$ of 14 K by adjusting its coordination environment (Ding et al., 2016). In 2022, Zheng et al. used carborane ligands to coordinate with rare earth ions to construct a series of rare earth metal-organic complexes; the terbium complexes performed better, becoming a new benchmark for Tb(III)-based SMMs (Jin et al., 2022). In the same year, they synthesized three examples of pentagonal bipyramid configuration Dy(III)-based SMMs by fixing the planar ligand and the balance anion unchanged and gradually fluorinating the axial alcohol-oxygen ligand (Ma et al., 2022). In addition, multi-core SMMs have also made some progress; but compared with single-core SMMs, the progress of multi-core SMMs is slow. In 2020, Tong et al. used the construction of magnetic functional units with suitable coordination geometry, and at the same time, magnetic coupling between spin carriers could be introduced to assemble high-performance multi-core SMMs with controllable structure and tunable functions (Huang et al., 2020). In the same year, Zheng et al. used alcohol amine

[1]School of Chemistry and Pharmaceutical Sciences, State Key Laboratory for Chemistry and Molecular Engineering of Medicinal Resources, Guangxi Normal University, Guilin 541004, P. R. China

[2]Guangxi Key Laboratory of Electrochemical and Magnetochemical Functional Materials, College of Chemistry and Bioengineering, Guilin University of Technology, Guilin 541004, P. R. China

[3]Lead contact

*Correspondence:
18317725515@163.com
(Z.-H.Z.),
fliangoffice@yahoo.com
(F.-P.L.),
gxnuchem@foxmail.com
(H.-H.Z.)

https://doi.org/10.1016/j.isci.2022.105285

ligands to prepare a series of 16-membered cyclic heterospin clusters composed of alternating Fe(III) and Ln(III) ions; the magnetic exchange between metal ions in {Fe$_8$Dy$_8$} ring molecules is ferromagnetic exchange, which plays a key role in enhancing the ring magnetic moment of dysprosium(III) (Zhang et al., 2020). In 2021, Tang et al. reported air-stable chiral SMMs with an anisotropy barrier over 1800 K, and high-performance SMMs are of great significance for the realization of SMMs in molecular-based magneto-electronic devices (Zhu et al., 2021). In 2022, Zheng et al. introduced a central fluorine bridge in a 3days-4f SMM, which strongly suppressed its quantum tunneling phenomenon at zero field; this work provides a basis for understanding the quantum tunneling process and designing a high remanence magnetism Ratio's SMMs offer a new powerful solution (Ling et al., 2022).

To design SMMs based on mononuclear complexes with superior performance and special magnetic behavior, the ligand field strength and topology of these complexes are controlled despite the metal center coordination configuration (Woodru et al., 2013; Guo et al., 2018a; Goodwin et al., 2017; Ding et al., 2016; Jin et al., 2022; Ma et al., 2022; Huang et al., 2020; Zhang et al., 2020; Zhu et al., 2021; Ling et al., 2022; Liu et al., 2018; Guo et al., 2018a, 2018a; Yu et al., 2022). However, developing effective strategies to break through the tremendous progress achieved in SMMs based on mononuclear complexes remains difficult (Zhang et al., 2020; Zhu et al., 2021; Ling et al., 2022; Liu et al., 2018; Lu et al., 2022). SMMs containing only one lanthanoid metal center may represent the lower size limit of molecular-based magnetic information storage materials (Guo et al., 2018b). This condition means that the specific arrangement of multiple mononuclear complex-based SMMs endows their magnetic axes a uniform directionality, and good SMM performance can be obtained (Orlova et al., 2022; Zhu et al., 2018; Habib and Lin, 2011; Wang et al., 2018). However, in a high-nucleation cluster structure, the disorder of the magnetic axis arrangement in the metal center greatly increases as the number of nuclei increases, making the structure disordered and causing the magnetic axes to cancel each other out (Wang et al., 2021a; Yu et al., 2021a). Therefore, designing and synthesizing highly nucleated lanthanoid clusters with SMM behavior are extremely difficult, and progress has been slow. The exploration of the self-assembly process and the study of the assembly mechanism have laid the foundation for the directional construction of high-nucleation clusters with specific arrangements (Zheng et al., 2018; Huang et al., 2022; Wang et al., 2019a). High-nucleation lanthanoid clusters typically undergo a multi-level assembly process from simple template motifs (Zhu et al., 2018; Du et al., 2020, 2022). Hence, designing rational template primitives and following specific assembly rules are two of the fastest and most efficient ways to construct high-nucleation lanthanoid clusters with specific properties.

Herein, we obtained a series of ns-4f heterometallic clusters (1–3) with triple-core building block as template primitives through the solvothermal reaction of o-vanillin derivative, Dy(OAc)$_3$·4H$_2$O, and alkali metal hydroxide under "one-pot" conditions (Scheme 1). Cluster 1 is formed by connecting two K(I) ions located at the upper and lower ends of the plane of Dy$_3$ with a triangular shape through $\mu_4$-O$^{2-}$ ions. Cluster 2 is formed by two metal center K(I) ions linking two vertically distributed Dy$_3$. Cluster 3 can be regarded as an open, cage-like structure with a large cavity formed by six Na(I) ions on a spherical surface connecting four triangular Dy$_3$ (Scheme 1). Notably, our clever introduction of alkali metal ions (K(I) or Na(I)) can effectively orient the triangular Dy$_3$ template motifs, so the rapid loss of performance of the SMMs of high-nucleation clusters is effectively prevented. Magnetic analysis showed that under a zero field, the imaginary part ($\chi''$) signals of clusters 1–3 exhibited frequency- and temperature-dependent behaviors, and obvious peaks were observed, indicating that they were all typical SMMs. As far as we know, this is the first time that high-nucleation cluster-based SMMs are constructed by connecting magnetic template elements through diamagnetic metal centers. In addition, cluster 3 is currently the highest nuclear ns-4f heterometallic cluster-based SMM. Notably, we captured the template motif Dy$_3$ of clusters 1–3 with the increase in high-resolution electrospray mass spectrometry (HRESI-MS) ion source energy. Clusters 1 and 3 and template motif Dy$_3$ had high stability. To our knowledge, this is the first time that HRESI-MS is used to explore the formation of ns-4f high-nucleation heterometallic clusters. This work opens a new horizon for the design and synthesis of ns-4f high-nucleation, heterometallic, cluster-based SMMs.

## RESULTS

### Structural analysis of clusters 1–3

In brief, 0.2 mmol Dy(OAc)$_3$·4H$_2$O, 0.2 mmol 3-ethoxysalicylaldehyde, and 0.4 mmol KOH were accurately weighed and dissolved in a mixed solvent of CH$_3$OH:CH$_3$CN = 1.5:0.5. Then, the mixed solution was placed under a solvothermal condition at 60°C for 48 h to obtain yellow bulk crystals (cluster 1). The single-crystal
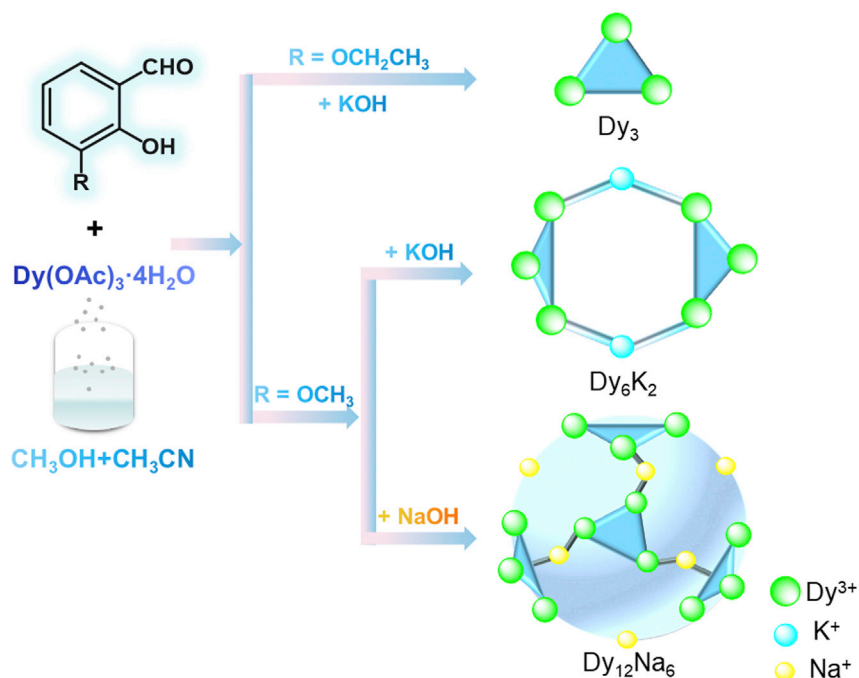
**Scheme 1. Schematic diagram of selecting Dy$_3$ as building block and adding diamagnetic alkali metal connection to obtain clusters 1–3**

X-ray diffraction (SCXRD) results showed that cluster **1** crystallized in the *C2/c* space group of the triclinic system (Table S1. Single-Crystal X-Ray Crystallography, Related to STAR method Details.). Negative dianion cluster **1** is composed of three metal-centered Dy(III) ions, two metal-centered K(I) ions, two $\mu_4$-O$^{2-}$ ions and three (L$^1$)$^{3-}$ ligands (see Figure 1A). Cluster **1** has two hydronium ions (H$_3$O$^+$) at the periphery to balance its charge. Negative trivalent ligand (L$^1$)$^{3-}$ reaction mechanism is that the disproportionation reaction occurs first, and 3-ethoxysalicylaldehyde is disproportionated to generate one molecule of 3-ethoxysalicylic acid and one molecule of 3-ethoxysalicylic alcohol (see Figure S1). Next, an acetal reaction occurs in the reaction system. 3-ethoxysalicylaldehyde undergoes an addition reaction with one molecule of 3-ethoxysalicyl alcohol to form an unstable hemiacetal, which is then dehydrated with another molecule of 3-ethoxysalicyl alcohol to form an acetal Product (Trimer-I, H$_3$L$^1$) (see Figure S1). The three metal center Dy(III) ions in cluster **1** were all located on the equatorial plane and can be regarded as an equilateral triangle. The three Dy(III) ions were located at the three vertices of the triangle, the two metal center K(I) ions were located at the upper and lower ends of the central triangle, and the metal centers Dy(III) and K(I) were bridged by O atoms to form a {Dy/K/O} cluster core (see Figure 1B). All coordinating O atoms on the three (L$^1$)$^{3-}$ ligands chelated the metal center Dy(III) ions and K(I) ions, and they were located in the periphery of the cluster core and tightly wrapped the cluster core. Moreover, all three ligands had the same ligand coordination mode: $\mu_4$-$\eta^1$:$\eta^2$:$\eta^1$:$\eta^1$:$\eta^2$:$\eta^1$:$\eta^2$:$\eta^1$ (Figure 1C). The metal centers Dy1, Dy2, and Dy3 had the same coordination environment, and the coordination atoms around them were eight oxygen atoms that originated from the ligands' H$_3$L$^1$ and $\mu_4$-O$^{2-}$ ions (see Figure S2A). *SHAPE* calculations revealed that their coordination configuration appeared like a muffin with a $C_s$ symmetric environment (see Table S3). The metal centers K1 and K2 also had the same coordination environment, and the coordination atoms around them were seven oxygen atoms derived from the ligands' H$_3$L$^1$ and $\mu_4$-O$^{2-}$ ions, respectively (see Figure S2B). *SHAPE* calculations demonstrated that their coordination configuration appeared as a capped octahedron with a $C_{3v}$ symmetric environment. All Dy-O bonds in cluster **1** were in the normal range (see Table S2).

Yellow bulk crystals (cluster **2**) were obtained by substituting the same amount of *o*-vanillin for 3-ethoxysalicylaldehyde and reacting under the same conditions as those for cluster **1** for 48 h. SCXRD structure analysis showed that cluster **2** crystallized in the *P*-1 space group of the triclinic system (see Table S1). Cluster **2** consisted of six Dy(III) ions, two K(I) ions, six (L$^2$)$^{2-}$ ligands with two protons removed, two $\mu_3$-OH$^-$ ions, and six OAc$^-$ ions. Every three Dy(III) ions in cluster **2** structure could be regarded as an equilateral triangle, and the two triangles were arranged vertically (see Figure 1D). Negative divalent
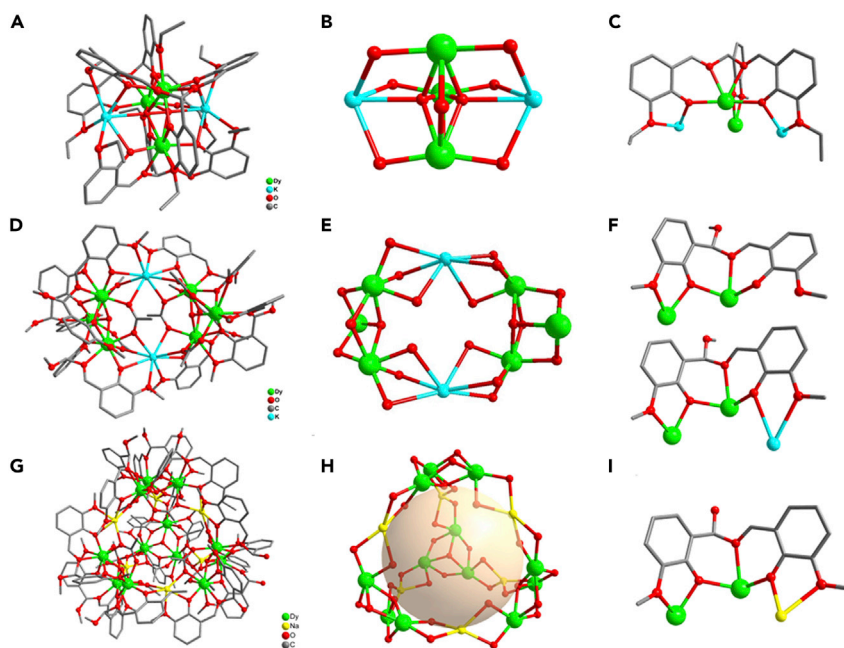
**Figure 1. Single crystal structures of clusters 1-3**
The crystal structure (A, D and G) and cluster core connection (B, E and H) diagram of clusters 1–3.; (C, F and I) The coordination patterns of the organic ligand (L$^1$)$^{3-}$ and (L$^2$)$^{2-}$ in clusters 1–3.

ligand (L$^2$)$^{2-}$ the first step is also a disproportionation reaction, the same as the first step to form the ligand H$_3$L$^1$. The acetal and dehydration reaction steps are next carried out in the reaction system (see Figure S1). First, an acetal reaction occurs in the reaction system. *o*-vanillin undergoes an addition reaction with solvent ethanol to form an unstable hemiacetal, which is then dehydrated with another molecule of 3-methoxysalicylic alcohol to form an acetal product (Dimer-II, H$_2$L$^2$). Cluster **2** had high symmetry, and the cluster core {Dy/K/O} could be regarded as formed by two metal center K(I) ions connecting two triangular Dy$_3$ (Figure 1E). Notably, the Dy$_3$ with a triangular shape in the structure of cluster **2** was similar to that in cluster **1**. Therefore, cluster **2** can be regarded as formed by two metal center K(I) ions linking the two clusters (**1**). The six (L$^2$)$^{2-}$ ligands in cluster **2** were all located in the periphery of the metal framework and chelated the central metal ion. In addition, the six ligands had two different coordination modes: $\mu_2$-$\eta^1$:$\eta^1$:$\eta^2$:$\eta^1$ and $\mu_3$-$\eta^1$:$\eta^2$:$\eta^1$:$\eta^2$:$\eta^1$ (see Figure 1F). The metal centers Dy1, Dy2, and Dy3 had the same coordination environment, and the coordination atoms around them were eight oxygen atoms derived from the ligands' H$_2$L$^2$ and $\mu_3$-OH$^-$ ions (see Figure S2C). *SHAPE* calculations showed that their coordination configuration appeared as a biaugmented trigonal prism with a $C_{2v}$ symmetric environment (see Table S4). The metal centers K1 and K2 had the same coordination environment, and the coordination atoms around them were eight oxygen atoms derived from the ligands' H$_2$L$^2$ and OAc$^-$ ions, respectively (see Figure S2D). *SHAPE* calculations demonstrated that their coordination configuration appeared as a square antiprism with a $D_{4d}$ symmetric environment (see Table S4). All Dy-O bonds in cluster **2** were in the normal range (see Table S2).

KOH was converted into the same amount of NaOH, and yellow bulk crystals (cluster **3**) were obtained under the same conditions as those for cluster **2** for 48 h. SCXRD structure analysis showed that cluster **3** was crystallized in the triclinic system's $P6_3$ space group (see Table S1). Cluster **3** consisted of 12 metal center Dy(III) ions, six Na(I) ions, 12 (L$^2$)$^{2-}$ ligands with two protons removed, two $\mu_3$-OH$^-$ ions, two $\mu_3$-O$^{2-}$ ions, and 12 OAc$^-$ ions (see Figure 1G). Cluster **3** had an open-cage structure with a large cavity, and 12 Dy(III) ions and six Na(I) ions were on the spherical surface. The {Dy/Na/O} cluster core of cluster **3** was formed by six metal-centered Na(I) ions connecting four triangular lattices formed by three metal-centered Dy(III) ions. Each Na(I) ion was connected to two triangular lattices (see Figure 1H). Notably, the 4 triangular lattices in cluster **3** were similar to those in cluster **1**. Therefore, cluster **3** can be regarded as formed by six Na(I) ions linking four clusters (**1**). The 12 (L$^2$)$^{2-}$ ligands in cluster **3** were located in the periphery of the metal framework and chelated the metal central ions, which played a protective role in the cluster core.

Furthermore, the 12 $(L^2)^{2-}$ ligands had the same coordination pattern: $\mu_3$-$\eta^1$:$\eta^2$:$\eta^1$:$\eta^2$:$\eta^1$ (see Figure 1I). The metal centers Dy1, Dy2, Dy3, and Dy4 possessed the same coordination environment, and the coordination atoms around them were eight oxygen atoms derived from the ligands' $H_2L^2$, $\mu_3$-OH$^-$, and OAc$^-$ ions (see Figure S2E). SHAPE calculations showed that their coordination configuration appeared as a biaugmented trigonal prism with a $C_{2v}$ symmetric environment (see Table S5). The coordination atoms around the six Na(I) metal central ions were six oxygen atoms, which were provided by the ligands' $H_2L^2$ and OAc$^-$ ions (see Figure S2F). SHAPE calculations showed that their coordination configuration was a trigonal prism with $D_{3h}$ symmetry (see Table S5). All Dy-O bonds in cluster **3** were in the normal range (see Table S2).

The $H_3L^1$ and $H_2L^2$ ligands had similar structures, and the ligand coordination patterns of clusters **2** and **3** were similar; thus, the infrared spectra of clusters **1–3** were basically the same (see Figure S3). The test results showed that the broad absorption peak around 3300 cm$^{-1}$ in the IR spectrum was attributed to the stretching vibration of $\nu$(HO–H) in the $H_2O$ molecules. The strong peak around 1640 cm$^{-1}$ was because of the C=N stretching vibration of the imine group (–C=N–). The strong peak around 1450 cm$^{-1}$ was attributed to the C=N and C=C stretching vibrations in the aromatic ring. The moderately intense absorption peak around 1210 cm$^{-1}$ was because of the stretching vibration between the alcoholic hydroxyl groups C–O (Wang et al., 2021b). Thermogravimetric analysis was conducted on clusters **1–3** in a flowing nitrogen atmosphere with a slow increment in temperature from 35°C to 1000°C at the rate of 5°C/min. Cluster **1** had three weightless processes. First, when the temperature was gradually increased from 35°C to 92°C, the weight loss rate was 6.0%. This process corresponded to the loss of two free $H_2O$ guest molecules, two free $H_3O$ molecules and two free $CH_3OH$ guest molecules (theoretical value of 5.75%). Second, when the temperature continued to rise to above 153°C, the weight loss rate was 12.8%. This process corresponded to the loss of four free $CH_3CN$ guest molecules (theoretical value of 12.74%). Lastly, cluster **1** was decomposed as the temperature continued to rise (see Figure S4A). Cluster **2** presented a weight loss of 14.2% before 190°C that corresponded to the loss of 12 free $CH_3CN$ guest molecules and three $H_2O$ guest molecules (theoretical value of 14.03%). Cluster **2** was decomposed as the temperature continued to rise (see Figure S4B). Meanwhile, Cluster **3** had two weightless processes. First, when the temperature was gradually increased from 35°C to 44°C, the weight loss rate was 1.85%. This process corresponded to the loss of three free $CH_3OH$ guest molecules and two free $H_2O$ guest molecules (theoretical value of 1.89%). Second, when the temperature continued to rise to above 170°C, the weight loss rate was 3.74%. This process corresponded to the loss of three free $CH_3CH$ guest molecules (3.69% theoretically). Cluster **3** was decomposed as the temperature continued to rise (see Figure S4C). In addition, the powder X-ray diffraction (PXRD) experimental values of Clusters **1–3** were compared with the theoretical values, and the results showed that they were all pure phases (see Figure S5).

## Magnetic analysis of clusters 1−3

The pure phases of clusters **1–3** were tested for variable temperature molar susceptibility from 300 K to 2 K under an external DC field of 1000 Oe (see Figure 2A−2C). At 300 K, the $\chi_m T$ value of cluster **1** was 43.79cm$^3$K mol$^{-1}$ ($^6H_{15/2}$, $S = 5/2$, $g = 4/3$, $J = 15/2$, $L = 5$), which was slightly higher than the theoretical value for three Dy(III) ions (*i.e.*, 42.51cm$^3$K mol$^{-1}$). When the temperature gradually decreased to about 100 K, the $\chi_m T$ of cluster **1** decreased slightly. When the temperature was lowered to 2 K, the $\chi_m T$ of cluster **1** rapidly decreased to 16.12cm$^3$K mol$^{-1}$, indicating the progressive depopulation of the excited Stark sublevels of Dy(III) ions and/or weak intra/inter-molecular magnetic interactions (Zhu et al., 2018; Dong et al., 2022). However, at 300 K, the $\chi_m T$ values for clusters **2** and **3** were 84.07 and 159.68cm$^3$K mol$^{-1}$ ($^6H_{15/2}$, $S = 5/2$, $g = 4/3$, $J = 15/2$, $L = 5$), respectively, both of which were lower than the theoretical values of six Dy(III) ions and 12 Dy(III) ions, respectively (85.02 and 170.04cm$^3$K mol$^{-1}$) (Patrascu et al., 2017; Wang et al., 2020). As the temperature gradually decreased to 140 K, the $\chi_m T$ values of Clusters **2** and **3** increased slowly. However, when the temperature was reduced by 40 K, the $\chi_m T$ values of clusters **2** and **3** decreased slowly. Notably, the $\chi_m T$ values of clusters **2** and **3** increased rapidly as the temperature approached 30 K. When the temperature decreased to 2 K, the $\chi_m T$ of clusters **2** and **3** rapidly increased to 95.86 and 169.32cm$^3$K mol$^{-1}$, respectively, which may have been caused by the decrease in the Stark sublevel of the Dy(III) excited state and the generated crystal field effect (Yu et al., 2021a, 2021b). Notably, an antiferromagnetic to ferrimagnetic transition occurred in clusters **1–3**. This phenomenon indicates that the strategy of using alkali metal ions to effectively separate and distribute trinuclear building blocks with annular magnetic moments provides a reference for regulating the magnetic properties of rare-earth clusters.
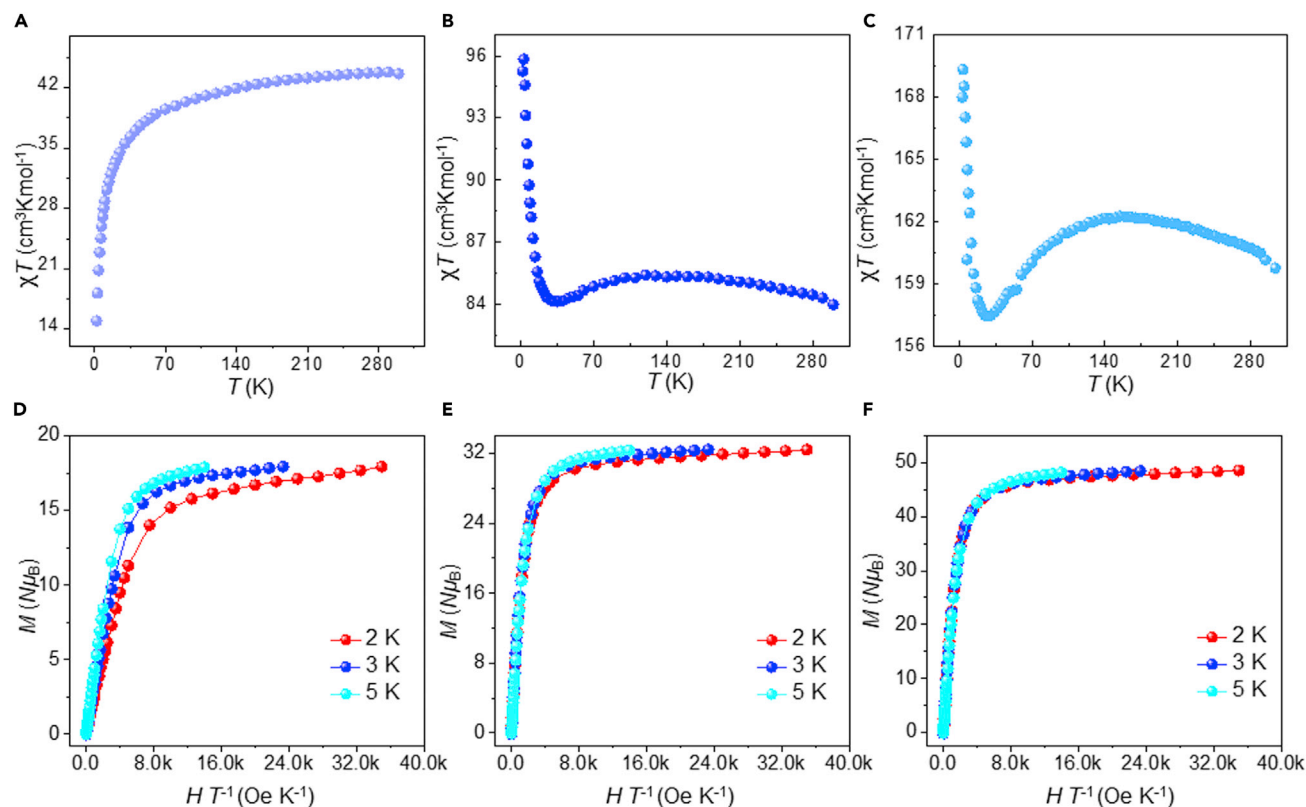
**Figure 2. Magnetic properties of clusters 1-3**
Temperature dependence of $\chi_m T$ for clusters 1–3 (A, B and C); $M$ versus $H/T$ plots of clusters 1–3 (D, E and F).

The field-dependent magnetization of clusters **1–3** was tested under an applied magnetic field of 0–7 T and a temperature range of 2–5 K. Then, $M$ versus $H/T$ curves were plotted (see Figures 2D−2F). Their measured magnetization at 2 K increased rapidly in the low-field region and gradually flattened out in the high-field region. When a static field of 9 kOe was reached, clusters **1–3** reached their maximum values of 18.69, 31.62, and 32.35 $N\beta$, respectively. The $M$ versus $H/T$ curves of clusters **1–3** at different temperatures showed insignificant non-overlapping. Compared with the $M$ versus $H/T$ curves of clusters **2** and **3**, those of cluster **1** showed a clearer non-overlap. All test results indicate that their Dy(III) ions may have low excited states and/or magnetic anisotropy (Du et al., 2020; Wang et al., 2021b; Layfield et al., 2010; Wang et al., 2012). As shown in Figure S6, the hysteresis loops of clusters **1–3** were not obvious at 2 K, which may be attributed to the existence of the crystal field effect and strong quantum tunneling effect.

The majority of existing triangle-based clusters exhibit interesting magnetic properties. We further tested their frequency- and temperature-dependent in-phase ($\chi'$) and out-of-phase ($\chi''$) alternating (ac) susceptibility to explore the slow magnetic relaxation behavior of clusters **1–3** (Hewitt et al., 2010; Lin et al., 2012; Zhu et al., 2018). As indicated in Figures 3 and S7, under a zero DC field, the out-of-phase signals of clusters **1–3** exhibited frequency- and temperature-dependent behaviors. In the temperature range of 3–16 K, cluster **1** had a clearly visible, temperature-dependent, out-of-phase AC magnetic susceptibility signal. In the tunable frequency range (1–1000 Hz), as the frequency increased, the out-of-phase peak gradually shifted to the high-temperature region, which is a typical feature of SMMs. Notably, in the range of 2–5 K, a weak double relaxation process existed for cluster **1**. Likewise, cluster **2** had a temperature-dependent, out-of-phase, AC magnetic susceptibility signal that exhibited a frequency-dependent behavior in the zero field, and a peak shape was observed. All test data indicated that cluster **2** was a typical example of SMM. In the temperature range of 2–12 K, cluster **3** with a large number of cores still had a clearly visible, temperature-dependent, out-of-phase AC magnetic susceptibility signal in the zero field, and in the tunable frequency range, the out-of-phase peak gradually shifted to the high-temperature region with increasing frequency, indicating that cluster **3** was a typical SMM. The out-of-phase ($\chi''$) signals of clusters **1–3** exhibited frequency- and temperature-dependent behaviors. However, we

found that clusters **1** and **2** exhibited out-of-phase AC magnetic susceptibility signals at $T = 6.5$ and 9.72 K, respectively, whereas cluster **3** preferentially showed out-of-phase AC magnetic susceptibility signals at $T = 10.27$ K (a higher temperature). Thus far, most SMMs have out-of-phase AC magnetic susceptibility signals in the low-temperature region, and reports on SMMs with out-of-phase AC magnetic susceptibility signals in the high-temperature region are rare.

As shown in Figure 3, the Cole–Cole plots of clusters **1–3** were relatively semicircular, and the fitted values were consistent with the generalized Debye model. Fitting parameter $\alpha$ was in the range of 0.04–0.51, 0.23–0.27, and 0.17–0.29 (see Tables S6−S8. Measurements of Magnetic, Related to STAR method Details.), indicating that cluster **1** had a large relaxation time distribution, as reflected by the wide AC peak of cluster **1**. The anisotropic energy barriers and magnetic relaxation times of clusters **1–3** were analyzed according to the thermal activation process of the Arrhenius law. The optimal results showed that under the zero DC field, the effective energy barriers and magnetic relaxation times of Clusters **1–3** were $U_{eff}$ = 45.5, 4.3, and 77.3 K and $\tau_0 = 2.4 \times 10^{-6}$, $1.7 \times 10^{-4}$, and $8.8 \times 10^{-8}$ s, respectively (see Figure S8). The relaxation mechanism of Dy(III)-based SMMs is usually complicated because of the existence of the Orbach process, the Raman process ($CT^n$), and the direct relaxation process ($AH^mT$) or quantum tunneling process (QTM) (Yu et al., 2022). For slow magnetic relaxation exhibited under a zero field, the direct relaxation process can be ignored. Therefore, when we fitted clusters **1–3** at all temperatures on the basis of these considerations, we obtained effective energy barriers and relaxation times of $U_{eff}$ = 53.6, 13.0, and 97.5 K and $\tau_0 = 1.4 \times 10^{-6}$, $1.2 \times 10^{-4}$, and $2.7 \times 10^{-8}$ s, respectively (see Figure S8).

Overall, clusters **1–3** exhibited a frequency-dependent behavior in the zero field, and clearly visible peaks were observed, indicating that they were typical SMMs. Compared with the molecular magnetic behaviors of clusters **1** and **3**, that of cluster **2** was slightly worse, which may be because of the fact that one of the two $Dy_3$ with a triangular shape in the structure of cluster **2** was located on the equatorial plane, and the other was perpendicular to the plane, resulting in the magnetic axes canceling each other out to exhibit poor molecular magnetic behavior. To the best of our knowledge, highly nucleated lanthanoid clusters (number of nuclei >10) with SMM characteristics have rarely been reported, and highly nucleated alkali metal lanthanoid-doped clusters with SMM characteristics are even rarer.

### Mass spectrometry analysis of clusters 1−3

HRESI-MS is a crucial technique for tracking species transformation in solutions and a powerful tool to study the stability of metal clusters in solutions (Zheng et al., 2018; Luo et al., 2020; Zhu et al., 2020b; Zhu et al., 2020a). However, exploration of the stability and assembly mechanisms of ns-4f clusters under mass spectrometry conditions is still rare (Mo et al., 2019; Ma et al., 2019). We dissolved a small sample of cluster **1–3** crystals in chromatographically pure DMF, diluted the solution extensively with readily vaporizable anhydrous methanol, and performed HRESI-MS testing. Data samples were collected in the $m/z$ range = 400–4000. The positive ion mode test results under the condition of ion source voltage of 0 eV showed that the main framework peaks of cluster **1** ($[Dy_3K_2(L^1)_3(O)_2(pos.)(solv.)]$ (pos. = positive ions, solv. = solvent) appeared at different $m/z$ ranges, and both showed the same valence state (+1) (see Figure 4). In addition, a series of molecular ion peaks containing $Dy_3K_2$ and $Dy_3K$ frameworks were observed. For example, at the position of $m/z = 2025.27$, the molecular ion peak with the highest intensity appeared, and the molecular formula was obtained by fitting as follows: $[Dy_3K(L^1)_3(OH)]^+(H_2O)_2]^{2+}$ (I, *calc.* 2025.34). The position at $m/z = 2030.28$ was calculated to be $[Dy_3K_2(L^1)_3(OH)(H^+)_2]$ (II, *calc.* 2030.30), the position at $m/z = 2047.25$ was $[Dy_3K_2(L^1)_3(OH)(H^+)](H_2O)$ (III, *calc.* 2047.30), the position at $m/z = 2063.25$ was $[Dy_3K_2(L^1)_3(OH)_2]^+(H_2O)$ (IV, *calc.* 2063.29), the position at $m/z = 2080.33$ was $[Dy_3K_2(L^1)_3(OH)_2]^+(H_2O)_2$ (V, *calc.* 2080.29), the position at $m/z = 2164.19$ was $[Dy_3K_2(L^1)_3(OH)_2(H)^+](H_2O)_3(CH_3OH)_2$ (VI, *calc.*2164.37), and the position at $m/z = 2309.19$ was $[Dy_3K_2(L^1)_3(OH)_2]^+(CH_3OH)_2(DMF)_2(H_2O)_3$(VII, *calc.*2309.46) (see Figure S9). Notably, with the continuous increase in HRESI-MS ion source voltage (0–100 eV), HRESI-MS under different ion source voltages could monitor the same molecular ion peaks as those under the 0 eV condition. However, as the ion source voltage was continuously increased, only the solvent molecules, the bridging ions around the nuclear cluster, and the alkali metal ions were replaced; the main frame did not undergo significant decomposition, indicating that cluster **1** had solution stability. These data indicate that cluster **1** was stable under HRESI-MS conditions with different ionization voltages.

We performed pressurized HRESI-MS testing on cluster **2** by using the same method. The overall framework of cluster **2** was decomposed even at 0 eV ion source voltage. The molecular ion peaks formed by
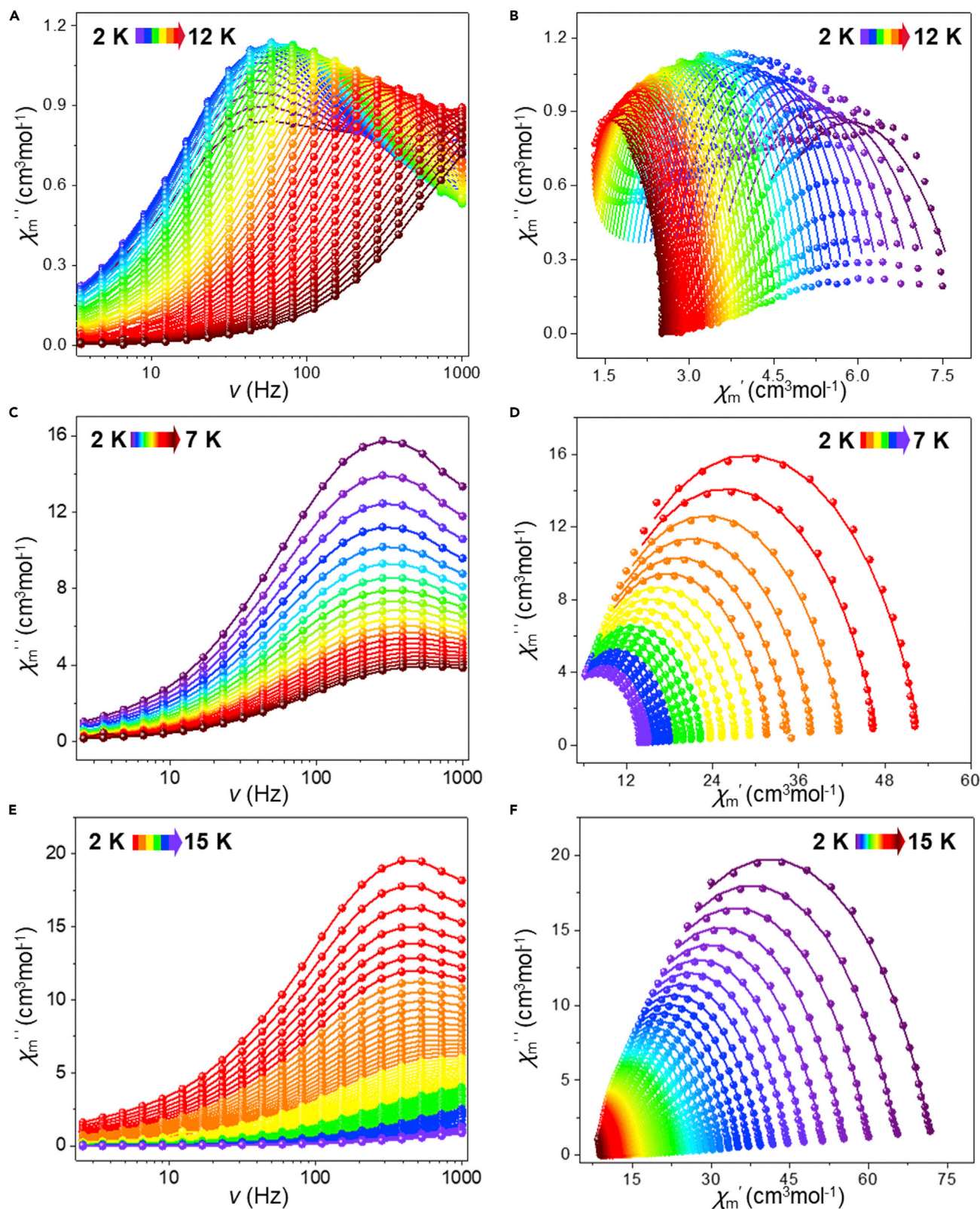
**Figure 3. Single-molecule magnets (SMMs) performance of clusters 1–3 under zero-field conditions**

Frequency and temperature dependence of the out-of-phase ($\chi''$) components under 0 Oe DC fields for clusters 1–3 (A, C and E); Cole–Cole plots for clusters 1–3 (B, D and F).
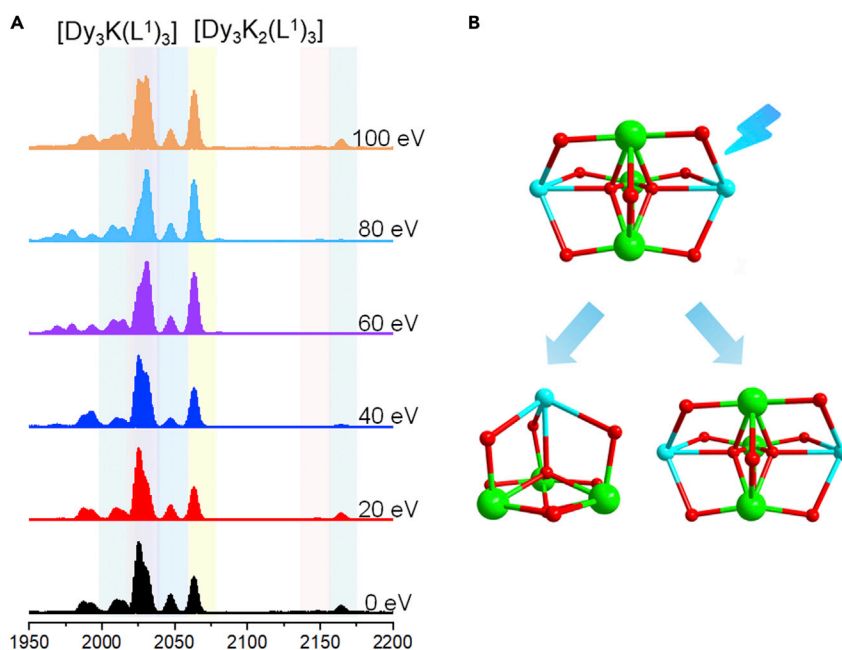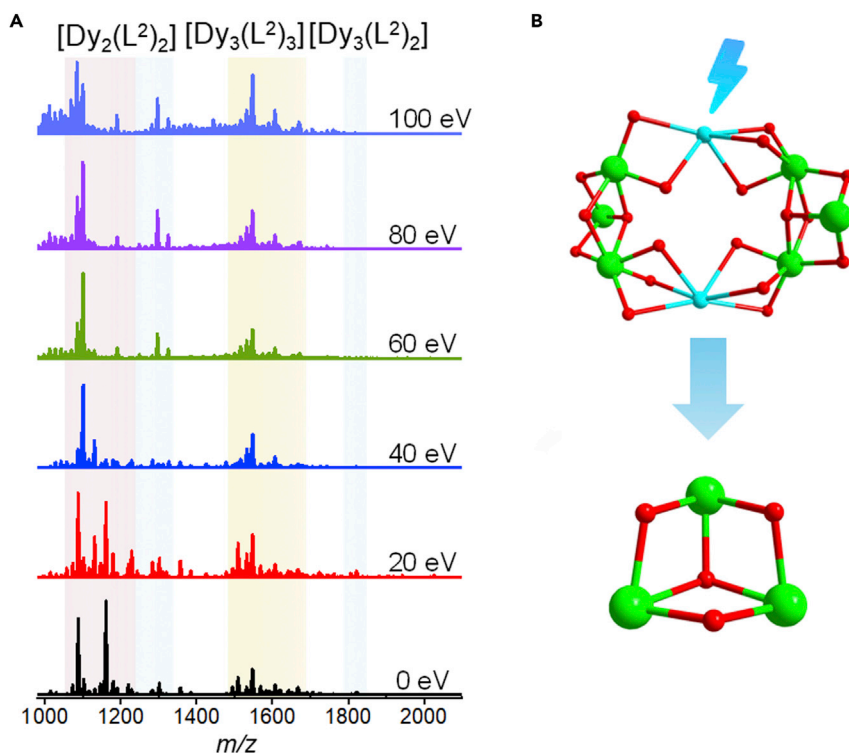
**Figure 4. High-resolution electrospray mass spectrometry (HRESI-MS) of cluster 1**

(A) Positive HRESI-MS spectra of cluster 1 in DMF (In-Source CID: 0, 20, 40, 60, 80, and 100 eV) and Schematic diagram of the mechanism of cluster 1 (B).

the fragmentation of cluster **2** appeared in the range of $m/z = 1088–1822$ and had the same valence state (+1) (see Figure 5). Within these ranges, by fitting the peaks, they can be assigned to $[Dy_3K(L^2)_2(OH)]^+(H_2O)_2$ (I, $exp. = 1088.15$, $calc.1088.13$), $[Dy_2K(L^2)_2(OH)(CH_3COO)]^+(CH_3CN)_3$ (II, $exp. = 1161.20$, $calc.1161.17$), $[Dy_3(L^2)_2(OH)(CH_3COO)]^+(CHCOOH)$ (III, $exp. = 1032.15$, $calc.1032.07$), $[Dy_3(L^2)_3(O)]^+(CH_3OH)(H_2O)$ (IV, $exp. = 1509.15$, $calc.1509.14$), $[Dy_3(L^2)_3(O)]^+(DMF)$ (V, $exp. = 1532.16$, $calc.1532.17$), $[Dy_3(L^2)_3(OH)]^+$ $(CH_3CN)(C_2H_5OH)$ (VI, $exp. = 1548.07$, $calc.1548.19$), $[Dy_3(L^2)_3(O)(CH_3COO)]^+(CH_3CN)(DMF)(H_2O)_2$ (VII, $exp. = 1668.13$, $calc.1668.22$), and $[Dy_3(L^2)_3(O)(CH_3COO)]^+(DMF)_2$ (VIII, $exp. = 1821.10$, $calc. 1821.22$) (see Figure S10). With increasing ion source voltage, the same molecular ion peaks as those at 0 eV were still observed at different ion source voltages. Alkali metal K(I) ions have weak coordination ability and easily disappear when a certain voltage is applied. Therefore, when we tested cluster **2** by using pressurized HRESI-MS, the K-O bond was broken, leaving only the $Dy_3$ fragment. These results show that $Dy_3$ fragments can exist stably in the solution state even under high-voltage bombardment, indicating that $Dy_3$ fragments have solution stability.

Likewise, we performed HRESI-MS on cluster **3** under the same conditions. When the ion source voltage was 0 eV, seven groups of molecular ion peaks were observed in the range of $m/z = 3310–3437$, and all of them showed the same valence state (+2) (see Figure 6). The seven groups of molecular ion peaks can be attributed to the following: $[Dy_{12}Na_6(L^2)_{12}(OH)_2(O)_2(CH_3COO)_{10}]^{2+}(H_2O)(CH_3OH)$ (I, $exp. = 3310.31$, $calc.3310.36$), $[Dy_{12}Na_6(L^2)_{12}(OH)_2(O)_2$ $(CH3COO)_{10}]^{2+}(CH_3OH)(H_2O)_2$ (II, $exp. = 3317.31$, $calc.3317.28$), $[Dy_{12}Na_6(L^2)_{12}(OH)_2(O)_2(CH_3COO)_{12}(H)]^{2+}(H_2O)$ (III, $exp. = 3353.81$, $calc.3353.84$), $[Dy_{12}Na_6(L^2)_{12}(OH)_2(O)_2(CH_3COO)_{10}]^{2+}(CH_3OH)_3(DMF)(H_2O)$ (IV, $exp. = 3376.84$, $calc.3376.89$), $[Dy_{12}Na_6(L^2)_{12}(OH)_2(O)_2(CH_3COO)_{12}]^{2+}(CH_3CN)_2(C_2H_5OH)$ (V, $exp. = 3406.38$, $calc.3406.33$), $[Dy_{12}Na_6(L^2)_{12}(OH)_2(O)_2(CH_3COO)_{12}(H)]^{2+}(CH_3OH)_2(CH_3CN)(H_2O)$ (VI, $exp. = 3413.33$, $calc.3413.34$), and $[Dy_{12}Na_6(L^2)_{12}(OH)_2(O)_2(CH_3COO)_{12}(H)]^{2+}(CH_3CN)_2(DMF)$ (VII, $exp. = 3436.86$, $calc.3436.92$) (see Figure S11). These molecular ion peaks were the main framework peaks of cluster **3** ($[Dy_{12}Na_6(L^2)_{12}(OH)_2(O)_2(CH_3COO)_{12}(-$ pos.)(solv.)]). In addition, a series of cationic fragments containing $[Dy_3(L^2)]$ were also observed. Examples included $[Dy_3(L^2)_3(O)(CH_3COO)]^+$ (I, $exp. = 1517.11$, $calc.1517.12$), $[Dy_3(L^2)_3(O)]^+(DMF)$ (II, $exp. = 1532.11$, $calc.1532.16$), $[Dy_3(L^2)_3(O)(CH_3COO)]^+(DMF)$ (III, $exp. = 1532.13$, $calc.1592.17$), $[Dy_3(L^2)_3(O)(CH_3COO)_2]^+(H_2O)_2$ (IV, $exp. = 1614.11$, $calc.1614.19$), $[Dy_3(L^2)_3(OH)(CH_3COO)_2]^+(CH_3OH)_2(H_2O)$ (V, $exp. = 1660.13$, $calc.1660.20$), $[Dy_3(L^2)_3(OH)(CH_3COO)_2]^+(CH_3OH)_3$ (VI, $exp. = 1674.13$, $calc.1674.22$), $[Dy_3(L^2)_3(OH)(CH_3COO)_3]^+(CH_3OH)$ $(DMF)_3$ (VII, $exp. = 1888.17$, $calc. 1888.34$), and $[Dy_3(L^2)_3(OH)(CH_3COO)_3]^+(CH_3OH)(DMF)_4$ (VIII, $exp. = 1961.18$, $calc. 1961.29$) (see Figure S12). The main framework peaks of cluster **3** could still exist stably even

**Figure 5. High-resolution electrospray mass spectrometry (HRESI-MS) of cluster 2**
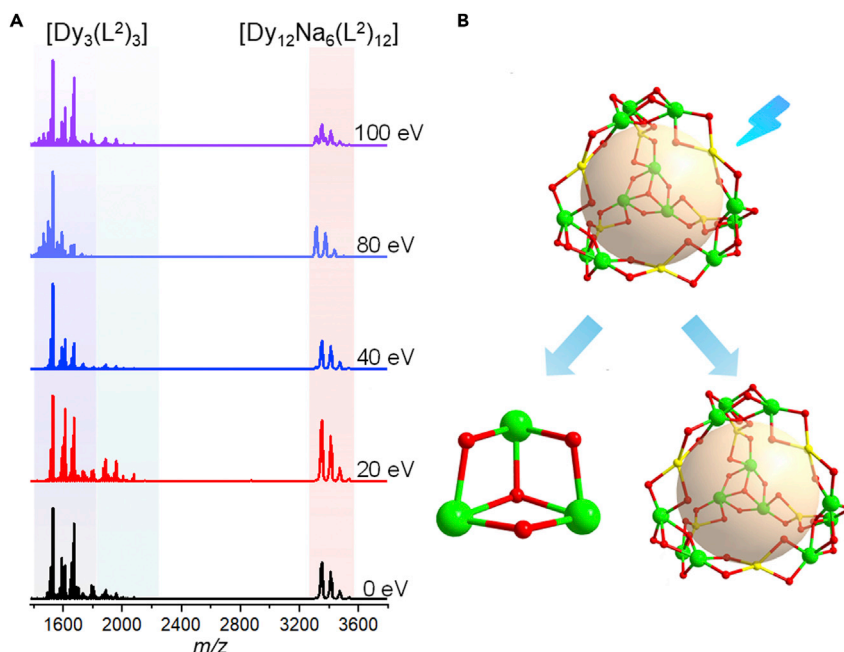Positive HRESI-MS spectra of cluster 2 in DMF (In-Source CID: 0, 20, 40, 60, 80, and 100 eV) (A) and Schematic diagram of the mechanism of cluster 2 (B).

with increasing HRESI-MS ion source voltage (0–100 eV), indicating that cluster **3** has solution stability. These data show that with increasing ion source voltage, only the solvent molecules in cluster **3**, the bridging ions around the core cluster, and the alkali metal ions were replaced without significant decomposition of the main backbone. Therefore, cluster **3** is stable under HRESI-MS conditions with different ionization voltages.

Overall, analysis of the HRESI-MS results showed that with the continuous increase in the ion source voltage (0–100 eV), clusters **1** and **3** could capture the molecular ion peaks of the main framework, indicating that both have good solution stability. Notably, $Dy_3$ fragments were detected in the pressurized HRESI-MS assay of clusters **1–3**. Therefore, in accordance with the analysis of the crystal structure and HRESI-MS test results, we can speculate that cluster **3** was formed by using $Dy_3$ as a building block through the connection of alkali metal ions. Previous research has shown that utilizing the building unit strategy is an efficient method for synthesizing rare-earth clusters. However, because molecular self-assembly usually involves a large number of molecules, determining how the building blocks are formed and screened is difficult. However, for the first time, we monitored the building block $Dy_3$ that formed alkali lanthanoid-doped cluster **3** via pressurized mass spectrometry. We speculated that the assembly mechanisms of clusters **1–3** are as follows: $Dy + K \rightarrow Dy_3K_2$, $Dy \rightarrow 2Dy_3 + K \rightarrow Dy_6K_2$, and $Dy \rightarrow 4Dy_3 + Na \rightarrow Dy_{12}Na_6$ (see Scheme 2). Therefore, clusters **1** and **2** can be regarded as intermediates of cluster **3** to a certain extent, and the acquisition of clusters **1** and **2** provides reliable evidence for the study of the self-assembly mechanism of cluster **3**.

## DISCUSSION

In conclusion, we used *o*-vanillin derivatives to react with $Dy(OAc)_3 \cdot 4H_2O$ under solvothermal conditions and employed alkali metal hydroxide to control the acidity of the reaction system and obtain a series of ns-4*f* heterometallic clusters (**1–3**). Cluster **1** was composed of triangular $Dy_3$ and two K(I) ions at the upper and lower ends of the plane. Cluster **2** consisted of two vertically oriented triangular $Dy_3$ ions connected by diamagnetic K(I) ions. Cluster **3** was an open, spherical cluster composed of six diamagnetic Na(I) ions connected to four triangular $Dy_3$. In the high-nucleation cluster structure, with the increase in the number of

**Figure 6. High-resolution electrospray mass spectrometry (HRESI-MS) of cluster 3**
Positive HRESI-MS spectra of cluster 3 in DMF (In-Source CID: 0, 20, 40, 80, and 100 eV) (A) and Schematic diagram of the mechanism of cluster 3 (B).

nuclei, the disorder of the magnetic axis arrangement of the metal center increased greatly such that the magnetic axes canceled each other. Hence, the high-nucleation clusters had difficulty exhibiting SMM behavior. We selected triangular template, which is poorly affected by directionality, as the building block and designed and synthesized n$s$-4$f$ heterometallic cluster-based SMM for the first time by using diamagnetic alkali metal connection. Cluster **3** is currently the highest nuclear n$s$-4$f$ heterometallic cluster-based SMM. Notably, the addition of alkali metal ions could effectively orient the single-molecule torus template moiety, thereby effectively preventing the rapid loss of SMM properties of the high-nucleation clusters. In addition, because of the large differences between alkali and lanthanoid metal ions in terms of radius, coordination mode, coordination range, and charge distribution, efficiently assembling n$s$-4$f$ heterometallic clusters was difficult. This work presents new ideas for the design and synthesis of n$s$-4$f$ heterometallic high-nucleation clusters. Notably, we used high-resolution electrospray mass spectrometry with different ion source energies to efficiently capture clusters **1**–**3** and the building blocks of Dy$_3$. Clusters **1** and **3** and the building blocks exhibited high stability with increasing ion source energy. To our knowledge, this is the first time that high-resolution electrospray mass spectrometry has been used to study the formation process of n$s$-4$f$ high-nucleation heterometallic clusters. This work provides a vivid example for the design and synthesis of n$s$-4$f$ high-nucleation heterometallic clusters and paves the way for the construction of high-nucleation cluster-based SMMs.

## Limitations of the study

In this study, although the ab initio calculation is of great significance to the study of magnetism; however, the structure is too bulky. We currently have no way to perform ab initio calculations.

## STAR★METHODS

Detailed methods are provided in the online version of this paper and include the following:

- KEY RESOURCES TABLE
- RESOURCE AVAILABILITY
  - Lead contact
  - Materials availability
  - Date and code availability
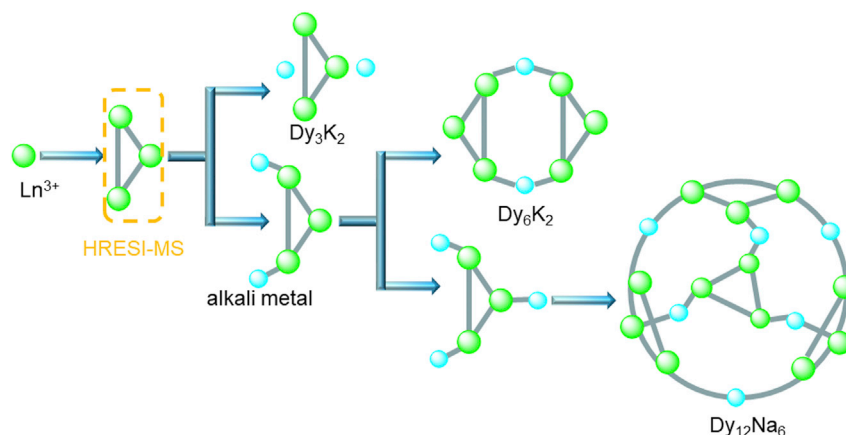
**Scheme 2. Schematic diagram of the assembly mechanism of clusters 1–3 using trinuclear building blocks with annular magnetic moments as templates**

- EXPERIMENTAL MODEL AND SUBJECT DETALS
  - The synthesis method
  - Valence calculations for Cluster 2
  - Valence calculations for Cluster 3
- METHOD DETAILS
  - Single-crystal X-Ray crystallography
  - Elemental analyses
  - Infrared spectra
  - Thermogravimetric analyses (TGA)
  - Powder X-Raydiffraction (PXRD)
  - HRESI-MS measurement
  - Measurements of Magnetic
- QUANTIFICATION AND STATISTICAL ANALYSIS

Consent for publication: All authors gave their consent for publication.

## AUTHOR CONTRIBUTIONS

Yun-Lan Li and Hai-Ling Wang: tested, collected and analyzed data for all clusters; Yun-Lan Li: writing-original draft; Xing-Lin Lu: synthesized clusters **1**–**3**; Zhong-Hong Zhu: conceived the aim idea of this work and revised original draft; Hua-Hong Zou and Fu-Pei Liang: provided financial support; Hua-Hong Zou: supervised and revised the manuscript. All authors discussed the results and commented on the manuscript.

## DECLARATION OF INTERESTS

The authors declare no competing interests.

## REFERENCES

Bogani, L., and Wernsdorfer, W. (2008). Molecular spintronics using single-molecule magnets. Nat. Mater. *7*, 179–186. https://doi.org/10.1142/97898142870050020.

Chen, Y.C., Liu, J.L., Ungur, L., Liu, J., Li, Q.W., Wang, L.F., Ni, Z.P., Chibotaru, L.F., Chen, X.M., and Tong, M.L. (2016). Symmetry-supported magnetic blocking at 20 K in pentagonal bipyramidal Dy(III) single-ion magnets. J. Am. Chem. Soc. *138*, 2829–2837. https://doi.org/10.1021/jacs.5b13584.

Ding, Y.S., Chilton, N.F., Winpenny, R.E.P., and Zheng, Y.Z. (2016). On approaching the limit of molecular magnetic anisotropy: a near-perfect pentagonal bipyramidal dysprosium(III) single-molecule magnet. Angew. Chem. Int. Ed. Engl. *55*, 16071–16074. https://doi.org/10.1002/anie.201609685.

Dong, H.M., Liu, Z.Y., Tang, H.M., Yang, E.C., Zhang, Y.Q., and Zhao, X.J. (2022). Slow relaxation of Dy(III) dalt. Dalton Trans. *51*, 1175–1181. https://doi.org/10.1039/d1dt03637h.

Du, M.H., Xu, S.H., Li, G.J., Xu, H., Lin, Y., Liu, W.D., Long, L.S., Zheng, L.S., and Kong, X.J. (2022). Modification of multi-component building blocks for assembling giant chiral lanthanide-titanium molecular rings. Angew.Chem. Int. Ed. Engl. *61*. e202116296. https://doi.org/10.1002/anie.202116296.

Du, M.H., Zheng, X.Y., Kong, X.J., Long, L.S., and Zheng, L.S. (2020). Synthetic protocol for assembling giant heterometallic hydroxide clusters from building blocks: rational design and efficient synthesis. Matter *3*, 1334–1349. https://doi.org/10.1016/j.matt.2020.06.020.

Durrant, J.P., Day, B.M., Tang, J., Mansikkamäki, A., and Layfield, R.A. (2022). Dominance of cyclobutadienyl over cyclopentadienyl in the crystal field splitting in dysprosium single-molecule magnets. Angew.Chem. Int. Ed. Engl. *61*. e202200525–e202200527. https://doi.org/10.1002/anie.202200525.

Goodwin, C.A.P., Ortu, F., Reta, D., Chilton, N.F., and Mills, D.P. (2017). Molecular magnetic hysteresis at 60 kelvin in dysprosocenium. Nature *548*, 439–442. https://doi.org/10.1038/nature23447.

Guo, F.S., Day, B.M., Chen, Y.C., Tong, M.L., Mansikkamäki, A., and Layfield, R.A. (2018a). Magnetic hysteresis up to 80 kelvin in a dysprosium metallocene single-molecule magnet. Science *362*, 1400–1403. https://doi.org/10.1126/science.aav0652.

Guo, F.S., He, M., Huang, G.Z., Giblin, S.R., Billington, D., Heinemann, F.W., Tong, M.L., Mansikkamäki, A., and Layfield, R.A. (2022). Discovery of a dysprosium metallocene single-molecule magnet with two high-temperature Orbach processes. Inorg. Chem. *61*, 6017–6025. https://doi.org/10.1021/acs.inorgchem.1c03980.

Guo, M., Zhang, Y.Q., Zhu, Z., and Tang, J. (2018b). Dysprosium compounds with hula-hoop-like geometries: the influence of magnetic anisotropy and magnetic interactions on magnetic relaxation. Inorg. Chem. *57*, 12213–12221. https://doi.org/10.1021/acs.inorgchem.8b01878.

Gupta, S.K., Rajeshkumar, T., Rajaraman, G., and Murugavel, R. (2016). An air-stable Dy(III) single-ion magnet with high anisotropy barrier and blocking temperature. Chem. Sci. *7*, 5181–5191. https://doi.org/10.1039/c6sc00279j+.

Habib, F., Lin, P.H., Long, J., Korobkov, I., Wernsdorfer, W., and Murugesu, M. (2011). The use of magnetic dilution to elucidate the slow magnetic. J. Am. Chem. Soc. *133*, 8830–8833.

Hewitt, I.J., Tang, J., Madhu, N.T., Anson, C.E., Lan, Y., Luzon, J., Etienne, M., Sessoli, R., and Powell, A.K. (2010). Coupling Dy3 triangles enhances their slow magnetic relaxation. Angew.Chem. Int. Ed. Engl. *49*, 6352–6356. https://doi.org/10.1002/anie.201002691.

Huang, G.Z., Ruan, Z.Y., Zheng, J.Y., Chen, Y.C., Wu, S.G., Liu, J.L., and Tong, M.L. (2020). Seeking magneto-structural correlations in easily tailored pentagonal bipyramid Dy(III) single-ion magnets. Sci. China Chem. *63*, 1066–1074. https://doi.org/10.1007/s11426-020-9746-x.

Huang, W., Chen, W., Bai, Q., Zhang, Z., Feng, M., and Zheng, Z. (2022). Anion-Guided stepwise assembly of high-nuclearity lanthanide hydroxide clusters. Angew. Chem. Int. Ed. Engl. *61*, e202205385. https://doi.org/10.1002/anie.202205385.

Jin, P.B., Yu, K.X., Luo, Q.C., Liu, Y.Y., Zhai, Y.Q., and Zheng, Y.Z. (2022). Tetraanionic arachno-carboranyl ligand imparts strong axiality to terbium(III) single-molecule magnets. Angew.Chem. Int. Ed. Engl. *61*. e202203285–e202203287. https://doi.org/10.1002/anie.202203285.

Ke, H., Xu, G.F., Guo, Y.N., Gamez, P., Beavers, C.M., Teat, S.J., and Tang, J. (2010). A linear tetranuclear dysprosium(iii) compound showing single-molecule magnet behaviour. Chem. Commun. *46*, 6057–6059. https://doi.org/10.1039/c0cc01067g.

Layfield, R.A., McDouall, J.J.W., Sulway, S.A., Tuna, F., Collison, D., and Winpenny, R.E.P. (2010). Influence of the N-bridging ligand on magnetic relaxation in an organometallic dysprosium single-molecule magnet. Chemistry *16*, 4442–4446. https://doi.org/10.1002/chem.201000158.

Lin, S.Y., Wernsdorfer, W., Ungur, L., Powell, A.K., Guo, Y.N., Tang, J., Zhao, L., Chibotaru, L.F., and Zhang, H.J. (2012). Coupling Dy3 triangles to maximize the toroidal moment. Angew. Chem. Int. Ed. Engl. *51*, 12767–12771. https://doi.org/10.1002/anie.201206602.

Ling, B.K., Zhai, Y.Q., Jin, P.B., Ding, H.F., Zhang, X.F., Lv, Y., Fu, Z., Deng, J., Schulze, M., Wernsdorfer, W., and Zheng, Y.-Z. (2022). Suppression of zero-field quantum tunneling of magnetization by a fluorido bridge for a "very hard" 3d-4f single-molecule magnet. Matter *5*, 3485–3498. https://doi.org/10.1016/j.matt.2022.07.009.

Liu, J., Chen, Y.C., Liu, J.L., Vieru, V., Ungur, L., Jia, J.H., Chibotaru, L.F., Lan, Y., Wernsdorfer, W., Gao, S., et al. (2016a). A stable pentagonal bipyramidal Dy(III) single-ion magnet with a record magnetization reversal barrier over 1000

K. J. Am. Chem. Soc. *138*, 5441–5450. https://doi.org/10.1021/jacs.6b02638.

Liu, J.L., Chen, Y.C., and Tong, M.L. (2018). Symmetry strategies for high performance lanthanide-based single-molecule magnets. Chem. Soc. Rev. *47*, 2431–2453. https://doi.org/10.1039/c7cs00266a.

Liu, K., Zhang, X., Meng, X., Shi, W., Cheng, P., and Powell, A.K. (2016b). Constraining the coordination geometries of lanthanide centers and magnetic building blocks in frameworks: a new strategy for molecular nanomagnets. Chem. Soc. Rev. *45*, 2423–2439. https://doi.org/10.1039/c5cs00770d.

Lu, J., Guo, M., and Tang, J. (2017). Recent developments in lanthanide single-molecule magnets. Chem. Asian J. *12*, 2772–2779. https://doi.org/10.1002/asia.201701032.

Lu, X.L., Wang, H.L., Peng, J.M., Zhu, Z.H., Bai, J., Zou, H.H., and Liang, F.P. (2022). Manipulation of mixed ligands to form single-layer and double-layer lanthanide clusters and their magnetic properties. Cryst. Growth Des. *22*, 2132–2138. https://doi.org/10.1021/acs.cgd.1c01179.

Luo, Z.R., Wang, H.L., Zhu, Z.H., Liu, T., Ma, X.F., Wang, H.F., Zou, H.H., and Liang, F.P. (2020). Assembly of $Dy_{60}$ and $Dy_{30}$ cage-shaped nanoclusters. Commun. Chem. *3*, 30–39. https://doi.org/10.1038/s42004-020-0276-3.

Ma, X.F., Wang, H.L., Zhu, Z.H., Li, B., Mo, K.Q., Zou, H.H., and Liang, F.P. (2019). Formation of nanocluster {Dy12} containing Dy-exclusive vertex-sharing [Dy4(μ3-OH)4] cubanes: via simultaneous multitemplate guided and step-by-step assembly. Dalton Trans. *48*, 11338–11344. https://doi.org/10.1039/c9dt01454c.

Ma, Y., Zhai, Y.Q., Luo, Q.C., Ding, Y.S., and Zheng, Y.Z. (2022). Ligand fluorination to mitigate the Raman relaxation of DyIII single-molecule magnets: a combined terahertz, far-IR and vibronic barrier model study. Angew. Chem. Int. Ed. Engl. *61*. e202206022. https://doi.org/10.1002/anie.202206022.

Meng, Y.S., Jiang, S.D., Wang, B.W., and Gao, S. (2016). Understanding the magnetic anisotropy toward single-ion magnets. Acc. Chem. Res. *49*, 2381–2389. https://doi.org/10.1021/acs.accounts.6b00222.

Mo, K.Q., Zhu, Z.H., Wang, H.L., Ma, X.F., Peng, J.M., Zou, H.H., Bai, J., and Liang, F.P. (2019). Substituents lead to differences in the formation of two different butterfly-shaped $Ni^{II}_2Dy^{III}_2$ clusters: structures and multistep assembly mechanisms. Dalton Trans. *48*, 16641–16649. https://doi.org/10.1039/c9dt03795k.

Orlova, A.P., Hilgar, J.D., Bernbeck, M.G., Gembicky, M., and Rinehart, J.D. (2022). Intuitive control of low-energy magnetic excitations via directed dipolar interactions in a series of Er(III)-Based complexes. J. Am. Chem. Soc. *144*, 11316–11325. https://doi.org/10.1021/jacs.2c03236.

Patrascu, A.A., Calancea, S., Briganti, M., Soriano, S., Madalan, A.M., Cassaro, R.A.A., Caneschi, A., Totti, F., Vaz, M.G.F., and Andruh, M. (2017). A chimeric design of heterospin 2p-3d, 2p-4f, and 2p-3d-4f complexes using a novel family of

paramagnetic dissymmetric compartmental ligands. Chem. Commun. *53*, 6504–6507. https://doi.org/10.1039/c7cc03236f.

Peng, J.M., Yu, Q.X., Zhu, Z.H., Liu, Z.Y., Lu, X.L., Zou, H.H., and Liang, F.P. (2021). Two diamond-shaped Dy4Complexes caused by different topological connections: structure and magnetism. Cryst.Growth Des. *21*, 6056–6063. https://doi.org/10.1021/acs.cgd.1c01094.

Pugh, T., Chilton, N.F., and Layfield, R.A. (2016). A low-symmetry dysprosium metallocene single-molecule magnet with a high anisotropy barrier. Angew. Chem. Int. Ed. Engl. *55*, 11082–11085. https://doi.org/10.1002/anie.201604346.

Ungur, L., Lin, S.Y., Tang, J., and Chibotaru, L.F. (2014). Single-molecule toroics in Ising-type lanthanide molecular clusters. Chem. Soc. Rev. *43*, 6894–6905. https://doi.org/10.1039/c4cs00095a.

Wang, H.F., Zhu, Z.H., Peng, J.M., Yin, B., Wang, H.L., Zou, H.H., and Liang, F.P. (2020). Multifunctional binuclear Ln(III) complexes obtained via in situ tandem reactions: multiple photoresponses to volatile organic solvents and anticounterfeiting and magnetic properties. Inorg. Chem. *59*, 13774–13783. https://doi.org/10.1021/acs.inorgchem.0c02193.

Wang, H.L., Liu, T., Zhu, Z.H., Peng, J.M., Zou, H.H., and Liang, F.P. (2021a). A series of dysprosium clusters assembled by a substitution effect-driven out-to-in growth mechanism. Inorg. Chem. Front. *8*, 2136–2143. https://doi.org/10.1039/d1qi00101a.

Wang, H.L., Liu, T., Zhu, Z.H., Peng, J.M., Zou, H.H., and Liang, F.P. (2021b). PH manipulates the assembly of a series of dysprosium clusters with subtle differences. Inorg. Chem. Front. *8*, 3134–3140. https://doi.org/10.1039/d1qi00371b.

Wang, H.L., Ma, X.F., Peng, J.M., Zhu, Z.H., Li, B., Zou, H.H., and Liang, F.P. (2019a). Tracking the stepwise formation of the dysprosium cluster (Dy$_{10}$) with multiple relaxation behavior. Inorg.Chem. *58*, 9169–9174. https://doi.org/10.1021/acs.inorgchem.9b00760.

Wang, H.L., Ma, X.F., Zhu, Z.H., Zhang, Y.Q., Zou, H.H., and Liang, F.P. (2019b). A series of dysprosium-based hydrogen-bonded organic frameworks (Dy-HOFs): thermally triggered off → on conversion of a single-ion magnet. Inorg. Chem. Front. *6*, 2906–2913. https://doi.org/10.1039/c9qi00582j.

Wang, W.M., Kang, X.M., Shen, H.Y., Wu, Z.L., Gao, H.L., and Cui, J.Z. (2018). Modulating single-molecule magnet behavior towards multiple magnetic relaxation processes through structural variation in Dy4 clusters. Inorg. Chem. Front. *5*, 1876–1885. https://doi.org/10.1039/c8qi00214b.

Wang, Y.X., Shi, W., Li, H., Song, Y., Fang, L., Lan, Y., Powell, A.K., Wernsdorfer, W., Ungur, L., Chibotaru, L.F., et al. (2012). A single-molecule magnet assembly exhibiting a dielectric transition at 470 K. Chem. Sci. *3*, 3366–3370. https://doi.org/10.1039/c2sc21023a.

Wernsdorfer, W., and Sessoli, R. (1999). Quantum phase interference and parity effects in magnetic molecular clusters. Science *284*, 133–135. https://doi.org/10.1016/s1063-5467(98)80003-x.

Woodruff, D.N., Winpenny, R.E.P., and Layfield, R.A. (2013). Lanthanide single-molecule magnets. Chem. Rev. *113*, 5110–5148. https://doi.org/10.1021/cr400018q.

Yu, S., Hu, H., Liu, D., Liang, Y., Liang, F., Yin, B., and Chen, Z. (2022). Structural and magnetic studies of six-coordinated Schiff base Dy(iii) complexes. Inorg. Chem. Front. *9*, 3059–3070. https://doi.org/10.1039/d2qi00356b.

Yu, S., Wang, H.L., Chen, Z., Zou, H.H., Hu, H., Zhu, Z.H., Liu, D., Liang, Y., and Liang, F.P. (2021a). Two decanuclear Dy$^{III}_x$Co$^{II}_{10-x}$ (x = 2, 4) nanoclusters: structure, assembly mechanism, and magnetic properties. Inorg.Chem. *60*, 4904–4914. https://doi.org/10.1021/acs.inorgchem.0c03814.

Yu, S., Zhang, Q.H., Chen, Z., Zou, H.H., Hu, H., Liu, D., and Liang, F.P. (2021b). Structure, assembly mechanism and magnetic properties of heterometallic dodecanuclear nanoclusters Dy$^{III}_4$M$^{II}_8$ (M = Ni, Co). Inorg. Chem. Front. *8*, 5214–5224. https://doi.org/10.1039/d1qi01051d.

Zhang, H.L., Zhai, Y.Q., Qin, L., Ungur, L., Nojiri, H., and Zheng, Y.Z. (2020). Single-molecule toroic design through magnetic exchange coupling. Matter *2*, 1481–1493. https://doi.org/10.1016/j.matt.2020.02.021.

Zhang, P., Guo, Y.N., and Tang, J. (2013). Recent advances in dysprosium-based single molecule magnets: structural overview and synthetic strategies. Coord. Chem. Rev. *257*, 1728–1763. https://doi.org/10.1016/j.ccr.2013.01.012.

Zheng, H., Du, M.H., Lin, S.C., Tang, Z.C., Kong, X.J., Long, L.S., and Zheng, L.S. (2018). Assembly of a wheel-like Eu$_{24}$Ti$_8$ cluster under the guidance of high-resolution electrospray ionization mass spectrometry. Angew. Chem. Int. Ed. Engl. *57*, 10976–10979. https://doi.org/10.1002/anie.201806757.

Zhu, Z., Zhao, C., Feng, T., Liu, X., Ying, X., Li, X.L., Zhang, Y.Q., and Tang, J. (2021). Air-stable chiral single-molecule magnets with record anisotropy barrier exceeding 1800 K. J. Am. Chem. Soc. *143*, 10077–10082. https://doi.org/10.1021/jacs.1c05279.

Zhu, Z.H., Ma, X.F., Wang, H.L., Zou, H.H., Mo, K.Q., Zhang, Y.Q., Yang, Q.Z., Li, B., and Liang, F.P. (2018). A triangular Dy3 single-molecule toroic with high inversion energy barrier: magnetic properties and multiple-step assembly mechanism. Inorg. Chem. Front. *5*, 3155–3162. https://doi.org/10.1039/c8qi01069b.

Zhu, Z.H., Peng, J.M., Wang, H.L., Zou, H.H., and Liang, F.P. (2020a). Assembly mechanism and heavy metal ion sensing of cage-shaped lanthanide nanoclusters. Cell Rep. Phys. Sci. *1*, 100165. https://doi.org/10.1016/j.xcrp.2020.100165.

Zhu, Z.H., Wang, H.F., Yu, S., Zou, H.H., Wang, H.L., Yin, B., and Liang, F.P. (2020b). Substitution effects regulate the formation of butterfly-shaped tetranuclear Dy(III) cluster and Dy-based hydrogen-bonded helix frameworks: structure and magnetic properties. Inorg. Chem. *59*, 11640–11650. https://doi.org/10.1021/acs.inorgchem.0c01496.

# STAR★METHODS

## KEY RESOURCES TABLE

| REAGENT or RESOURCE | SOURCE | IDENTIFIER |
| --- | --- | --- |
| o-vanillin | Sahn chemical technology gmbh | CAS:148-53-8 |
| 3-Ethoxysalicylaldehyde | Sahn chemical technology gmbh | CAS:492-88-6 |
| $Dy(OAc)_3 \cdot 4H_2O$ | Aladdin Reagent Co., Ltd. | CAS:15,280-55-4 |
| KOH | Aladdin Reagent Co., Ltd. | CAS:1310-58-3 |
| NaOH | Sahn chemical technology gmbh | CAS:1310-73-2 |
| Methanol | Sahn chemical technology gmbh | CAS:67-56-1 |
| Acetonitrile | Sahn chemical technology gmbh | CAS:75-05-8 |

## RESOURCE AVAILABILITY

### Lead contact

Further information and requests for resources and reagents should be directed to and will be fulfilled by the Lead Contact, Hua-Hong Zou (gxnuchem@foxmail.com).

### Materials availability

All unique/stable reagents generated in this study are available from the lead contact with a completed Materials Transfer Agreement. This study did not generate additional unique reagents.

### Date and code availability

- The authors declare that the data supporting the findings of this study are available within the article and the supplemental information. All other data (e.g., CIF, INS, etc.) are available from the lead contact on reasonable request. The Cambridge Crystallographic Data Center (CCDC) reference numbers are 2,182,566–2182568 for 1–3. The crystallographic data sheet for this work has been provided in the PDF of Supporting Information (Tables S1 and S2).

- This article does not report original codes.

- Any additional information required to reanalyze the data reported in this article is available from the lead contact on request.

## EXPERIMENTAL MODEL AND SUBJECT DETALS

No experimental model exists for this work.

### The synthesis method

#### Synthesis of cluster 1

$([Dy_3K_2(L^1)_3(\mu_4\text{-}O)_2](H_3O)(H_2O)_2(CH_3OH)_2(CH_3CN)_4)$: Add 0.2 mmol (0.0332 g) 3-ethoxysalicylaldehyde, 0.4 mmol (0.0224 g) potassium hydroxide and 0.2 mmol $Dy(OAc)_3 \cdot 4H_2O$ (0.0822 g), 1.5 mL $CH_3OH$ and 0.5 mL $CH_3CN$ were added in a pyrex tube. The tube was shaken and sonicated for 15 min. We placed the sealed Pyrex tube in an oven at 60°C, took it out two days later, slowly allowed to cool to room temperature and precipitated to form yellow lumpy crystals. The yield was about 34% (calculated with the amount of $Dy(OAc)_3 \cdot 4H_2O$).

#### Valence calculations for Cluster 1

Three metal center Dy(III) ions: positive valence (+3) ✖ 3 = 9.

Two metal center K(I) ions: positive valence (+1) ✖ 2 = 2.

Twofree hydrated $(H_3O)^+$ ions: positive (+1) ✖ 2 = 2.

Three deprotonated ligands $(L^1)^{3-}$: negative valence (−3) ✖ 3 = −9.

Two bridged $\mu_4$-$O^{2-}$ ions: negative valence $(-2) \times 2 = -4$.

Sum: $9 + 2 + 2 – 9 – 4 = 0$.

*Synthesis of cluster 2*

$([Dy_6K_2(L^2)_6(\mu_3\text{-}OH)_2(OAc)_6](H_2O)_3(CH_3CN)_{12})$: The procedure was similar to that of cluster 1, except that except that 3-ethoxysalicylaldehyde by *o*-vanillin. The yield is about 33% (calculated with the amount of $Dy(OAc)_3 \cdot 4H_2O$).

## Valence calculations for Cluster 2

Six metal center Dy(III) ions: positive valence $(+3) \times 6 = 18$.

Two metal center K(I) ions: positive valence $(+1) \times 2 = 2$.

Six deprotonated ligands $(L^2)^{2-}$: negative valence $(-2) \times 6 = -12$.

Two bridged $\mu_3$-$OH^-$ ions: negative valence $(-1) \times 2 = -2$.

Six $OAc^-$ ions: negative valence $(-1) \times 6 = -6$.

Sum: $18 + 2 – 12 – 2 – 6 = 0$.

*Synthesis of cluster 3*

$([Dy_{12}Na_6(L^2)_{12}(\mu_3\text{-}OH)_2(\mu_3\text{-}O)_2(OAc)_{12}](H_2O)_2(CH_3OH)_3(CH_3CN)_3)$: The procedure was similar to that of cluster 2, except that potassium hydroxide by sodium hydroxide. The yield is about 34% (calculated with the amount of $Dy(OAc)_3 \cdot 4H_2O$).

## Valence calculations for Cluster 3

12 metal center Dy(III) ions: positive valence $(+3) \times 12 = 36$.

Six metal center Na(I) ions: positive valence $(+1) \times 6 = 6$.

12 deprotonated ligands $(L^2)^{2-}$: negative valence $(-2) \times 12 = -24$.

Two bridged $\mu_3$-$OH^-$ ions: negative valence $(-1) \times 2 = -2$.

Two bridged $\mu_3$-$O^{2-}$ ions: negative valence $(-2) \times 2 = -4$.

$12 OAc^-$ ions: negative valence $(-1) \times 12 = -12$.

Sum: $36 + 6 – 24 – 2 – 4 – 12 = 0$.

## METHOD DETAILS

### Single-crystal X-Ray crystallography

Diffraction data for the complex were collected on a Bruker SMART CCD diffractometer (Cu-K$\alpha$ radiation and $\lambda$ = 1.54 Å) in $\Phi$ and $\omega$ scan modes. The structures were solved by direct methods, followed by difference Fourier syntheses, and then refined by full-matrix least-squares techniques on F2 using *SHELXL*. All other non-hydrogen atoms were refined with anisotropic thermal parameters. Hydrogen atoms were placed at calculated positions and isotopically refined using a riding model. Table S1 (Single-Crystal X-Ray Crystallography, Related to STAR Method Details.) summarizes X-ray crystallographic data and refinement details for the complexes. The CCDC reference numbers are 2,182,566–2182568 for 1–3.

### Elemental analyses

Elemental analyses for C, N, and H were performed on a varia MICRO cube.

Elemental analysis of cluster 1: theoretical value: C, 46.65%; H, 4.94%; N, 2.39%; experimental value: C, 46.54%; H, 4.88%; N, 2.32%.

Elemental analysis of cluster 2: theoretical value: C, 46.65%; H, 4.95%; N, 2.39%; experimental value: C, 46.58%; H, 4.88%; N, 2.34%.

Elemental analysis of cluster 3: theoretical value: C, 41.34%; H, 4.03%; N, 0.60%; experimental value: C, 41.28%; H,3.97%; N, 0.56%.

## Infrared spectra

Infrared spectra were recorded by transmission through KBr pellets containing *ca.* 0.5% of the complexes using a PE Spectrum FT-IR spectrometer (400–4,000 cm$^{-1}$) (Figure S3).

Infrared spectrum data of cluster 1: 3439(m), 2930(w), 2841(w), 1580(s), 1462(s), 1334(w), 1215(m), 1065(s), 929(w), 852(m), 733(s), 652(w), 603(w), 504(w), 435(w).

Infrared spectrum data of cluster 2: 3439(m), 2930(w), 2841(w), 1580(s), 1462(s), 1334(w), 1215(m), 1065(s), 929(w), 852(m), 733(s), 652(w), 603(w), 504(w), 435(w).

Infrared spectrum data of cluster 3: 3259(m), 1647(s), 1551(w), 1447(s), 1310(m), 1207(s), 1074(w), 937(w), 857(m), 729(s), 657(w), 554(w).

## Thermogravimetric analyses (TGA)

Thermogravimetric analyses (TGA) were conducted in a flow of nitrogen at a heating rate of 5°C/min using a NETZSCH TG 209 F3 (Figure S4).

## Powder X-Raydiffraction (PXRD)

Powder X-ray diffraction (PXRD) spectra were recorded on either a D8 Advance (Bruker) diffractometer at 293 K (Mo-K$\alpha$). The samples were prepared by crushing crystals and the powder placed on a grooved aluminum plate. Diffraction patterns were recorded from 5° to 55° at a rate of 5° min$^{-1}$ (Figure S5).

## HRESI-MS measurement

HRESI-MS measurements were conducted at a capillary temperature of 275°C. Aliquots of the solution were injected into the device at 0.3 mL/h. The mass spec-trometer used for the measurements was a ThermoExactive, and the data were collected in positive and negative ion modes. The spectrometer was previously calibrated with the standard tune mix to give a precision of ∼2 ppm within the region of 200–7,500 *m/z*. The capillary voltage was 50 V, the tube lens voltage was 150 V, and the skimmer voltage was 25 V (Figures 4–6 and S9–S12).

## Measurements of Magnetic

Measurements of magnetic susceptibility were carried out within the temperature range of 2–300 K using a Quantum Design MPMS SQUID magnetometer equipped with a 7 T magnet. The diamagnetic corrections for these complexes were estimated using Pascal's constants, and magnetic data were corrected for diamagnetic contributions of the sample holder (Figures 2 and 3 and Figures S6–S8).

## QUANTIFICATION AND STATISTICAL ANALYSIS

Using Diamond to map the structure (Figures 1 and S1); Origin 8 to perform data processing on magnetic data, infrared, thermogravimetric, and PXRD (Figures 2–6 and S3–S12); Olex 2 performs structural elucidation of clusters 1–3.